

Spatial Separation of Cocatalysts on Z-Scheme Organic/Inorganic Heterostructure Hollow Spheres for Enhanced Photocatalytic H₂ Evolution and In-Depth Analysis of the Charge-Transfer Mechanism

Hyun Sik Moon, Kai-Chi Hsiao, Ming-Chung Wu, Yongju Yun, Yung-Jung Hsu, and Kijung Yong*

A Z-scheme heterojunction with spatially separated cocatalysts is proposed for overcoming fundamental issues in photocatalytic water splitting, such as inefficient light absorption, charge recombination, and sluggish reaction kinetics. For efficient light absorption and interfacial charge separation, Z-scheme organic/inorganic heterojunction photocatalysts are synthesized by firmly immobilizing ultrathin g-C₃N₄ on the surface of TiO₂ hollow spheres via electrostatic interactions. Additionally, two cocatalysts, Pt and IrO_x, are spatially separated along the Z-scheme charge-transfer pathway to enhance surface charge separation and reaction kinetics. The as-prepared Pt/g-C₃N₄/TiO₂/IrO_x (PCTI) hollow sphere photocatalyst exhibits an exceptional H₂ evolution rate of 8.15 mmol h⁻¹ g⁻¹ and a remarkable apparent quantum yield of 24.3% at 330 nm in the presence of 0.5 wt% Pt and 1.2 wt% IrO_x cocatalysts on g-C₃N₄ and TiO₂, respectively. Photoassisted Kelvin probe force microscopy is used to systematically analyze the Z-scheme charge-transfer mechanism within PCTI. Furthermore, the benefits of spatially separating cocatalysts in the PCTI system are methodically investigated in comparison to randomly depositing them. This work adequately demonstrates that the combination of a Z-scheme heterojunction and spatially separated cocatalysts can be a promising strategy for designing high-performance photocatalytic platforms for solar fuel production.

1. Introduction

Photocatalytic water splitting into clean hydrogen fuel is regarded as one of the most promising avenues to solving the energy and environmental crises.^[1-4] However, photocatalytic water splitting has a relatively low solar-to-hydrogen conversion, which is significantly below the required standard for practical applications.^[5,6] The low efficiency of photocatalytic water splitting is attributed to the following issues in the main steps: i) inefficient utilization of sunlight, ii) inefficient separation and transfer of photogenerated charge carriers, and iii) sluggish kinetics of the surface reactions.^[7-9] Hence, designing and fabricating a photocatalyst that broadens light absorption and simultaneously stimulates charge-carrier separation/transfer efficiency and reaction kinetics for water splitting are highly desirable.

The construction of heterostructures with two types of semiconductors has been demonstrated to be an effective

H. S. Moon, K. Yong
Surface Chemistry Laboratory of Electronic Materials
Department of Chemical Engineering
Pohang University of Science and Technology (POSTECH)
Pohang 37673, Republic of Korea
E-mail: kyong@postech.ac.kr

K.-C. Hsiao, M.-C. Wu
Department of Chemical and Materials Engineering
College of Engineering
Chang Gung University
Taoyuan 33302, Taiwan
K.-C. Hsiao, M.-C. Wu
Green Technology Research Center
Chang Gung University
Taoyuan 33302, Taiwan

Y. Yun
Nanocatalysis and Surface Science Laboratory
Department of Chemical Engineering
Pohang University of Science and Technology (POSTECH)
Pohang 37673, Republic of Korea

Y.-J. Hsu
Department of Materials Science and Engineering
National Yang Ming Chiao Tung University
Hsinchu 30010, Taiwan

Y.-J. Hsu
Center for Emergent Functional Matter Science
National Yang Ming Chiao Tung University
Hsinchu 30010, Taiwan

 The ORCID identification number(s) for the author(s) of this article can be found under <https://doi.org/10.1002/adma.202200172>.

DOI: 10.1002/adma.202200172

method for improving the performance of solar water splitting by enhancing charge separation at the interface.^[10–14] The Z-scheme heterostructure, in particular, has attracted significant attention because the photoexcited electrons and holes accumulate in one semiconductor with a more negative position in the conduction band (CB) and in the other semiconductor with a more positive position in the valence band (VB), respectively.^[15–19] Such a heterojunction simultaneously ensures enhanced light absorption and accelerated charge separation in the bulk phase. In addition to the matching band structures of the two semiconductors, the intimate interfacial contact between them plays a crucial role in promoting Z-scheme charge transfer across the heterojunction interface.^[15]

The use of cocatalysts has also been substantiated to be an effective method for stimulating the surface reaction kinetics because it can reduce the activation energy of reduction and oxidation reactions.^[20–22] Therefore, various noble metals, such as Pt, Ru, and Au, and metal oxides, such as CoO_x, IrO_x, and MnO_x, have been extensively investigated for photocatalytic water splitting.^[23–26] However, loading dual cocatalysts with a random distribution may increase the possibility of surface recombination and backward reactions due to an arbitrary flow direction of charge carriers.^[27–30] To address this issue, several studies have been conducted on the spatial separation of reduction and oxidation cocatalysts that can effectively trap photo-generated electrons and holes at opposite positions.^[27–29,31,32] Furthermore, to compensate for the insufficient contribution of spatially separated cocatalysts to bulk recombination,^[33–35] several studies have also been conducted on their cooperation with heterostructures, particularly type II.^[30,31,36] However, the sacrificed redox powers as a result of the descending charge-transfer direction of type II heterostructures may have compromised the effectiveness of such a cooperation. Instead, the vectorial charge-transfer pathway of Z-scheme heterostructures can ensure pronounced charge separation yet still retain high redox powers, which can work cooperatively with spatially separated cocatalysts to achieve breakthrough. Nevertheless, the synergetic effect of the spatial separation of cocatalysts and Z-scheme heterostructures on the performance of solar water splitting has not yet been fully exploited.

In this study, a Pt/g-C₃N₄/TiO₂/IrO_x (PCTI) heterostructure hollow sphere was designed and synthesized by considering the collaboration of Z-scheme heterostructures and the spatial separation of cocatalysts for the first time. Ultrathin g-C₃N₄ was firmly anchored on the surface of TiO₂ hollow spheres via strong electrostatic interactions, producing an intimate interfacial contact between the heterojunction and allowing the Z-scheme charge-transfer pathway to effectively separate charges in the bulk phase. In addition, the spatially separated Pt and IrO_x cocatalysts drove and trapped electrons and holes near the surface, respectively, causing them to flow in opposite directions, which restrained surface recombination and accelerated the reduction and oxidation reaction kinetics. Furthermore, g-C₃N₄ acted as a sensitizer, enhancing visible-light absorption. The PCTI system was analyzed using photoassisted Kelvin probe force microscopy (photo-KPFM) to unambiguously validate the Z-scheme charge-transfer mechanism and charge-trapping scenarios by cocatalysts. Combining advantages such as broader light absorption, efficient charge separation/transfer in

the bulk phase and at the surface, and enhanced surface reaction kinetics, the PCTI hollow sphere photocatalyst exhibited an exceptional photocatalytic hydrogen evolution performance of 8.15 mmol g⁻¹ h⁻¹.

2. Results and Discussion

The PCTI photocatalyst was synthesized using a hard template and etching method (Figure 1a). An oxidation cocatalyst, IrO_x, was anchored on the external surface of SiO₂ nanospheres to initiate the synthesis. Thereafter, TiO₂ and g-C₃N₄ layers were sequentially deposited on the IrO_x-loaded SiO₂ spheres via electrostatic attractions, resulting in TiO₂/IrO_x/SiO₂ (TIS) and g-C₃N₄/TiO₂/IrO_x/SiO₂ (CTIS) nanospheres. The deposition of the g-C₃N₄ layer was accompanied by a thin layer and partial aggregations. Pt, a reduction cocatalyst, was selectively deposited on the g-C₃N₄ surface on the outmost of the CTIS core-shell structure using the visible-light photodeposition method to form Pt/g-C₃N₄/TiO₂/IrO_x/SiO₂ (PCTIS). Finally, the PCTI hollow spheres were obtained after the SiO₂ core was removed using the NaOH etching process. Each step of the structure evolution is characterized via the scanning electron microscopy (SEM) and transmission electron microscopy (TEM) images in Figures S2–S4 (Supporting Information).

The morphology and structure of the PCTI hollow spheres were investigated using TEM and electron energy loss spectroscopy (EELS). The TEM image of PCTI in Figure 1b confirms the structure of the hollow spheres with a diameter of ≈600 nm. The PCTI particles have a uniform morphology, with an average shell thickness of 30 nm (Figure S5, Supporting Information) and a TiO₂ layer thickness of 22 nm (Figure S6, Supporting Information). Accordingly, the thickness of the g-C₃N₄ and Pt layer, which is mainly composed of ultrathin g-C₃N₄, is calculate

d as 8 nm. Figure S7 (Supporting Information) shows the high-angle annular dark-field scanning transmission electron microscopy (HAADF-STEM) image of TiO₂/IrO_x (TI) hollow spheres, with the IrO_x particles in bright contrast. Additionally, point scan energy-dispersive spectroscopy further confirmed that the IrO_x particles on the inner TiO₂ surface remained intact after the etching process (Figure S8, Supporting Information). The PCTI structure was further investigated using high-resolution TEM (HRTEM), as shown in Figure 1c. The outer and inner layers have lattice spacings of 0.327 ± 0.01 and 0.350 ± 0.01 nm, respectively, which are in good agreement with the (002) and (101) planes of g-C₃N₄ and anatase TiO₂, respectively. The dark particles on g-C₃N₄ have a lattice spacing of 0.211 ± 0.02 nm, which can be assigned to the Pt (111) plane. According to the statistical analysis of the particle size distribution and X-ray photoelectron spectroscopy (XPS), the Pt particles have an average size of 2.46 nm as the metallic Pt⁰ state^[37] (Figure S9, Supporting Information), while the IrO_x particles have an average size of 5.52 nm as the mixed-valence oxide state^[38] (Figure S10, Supporting Information). Figure 1d illustrates the EELS mapping of the Ti, Ir, N, and Pt signals, demonstrating that the Ti, N, and Pt distribution is consistent with the morphology shown in Figure 1b. However, the distribution of N and Pt is less dense than that of Ti, indicating

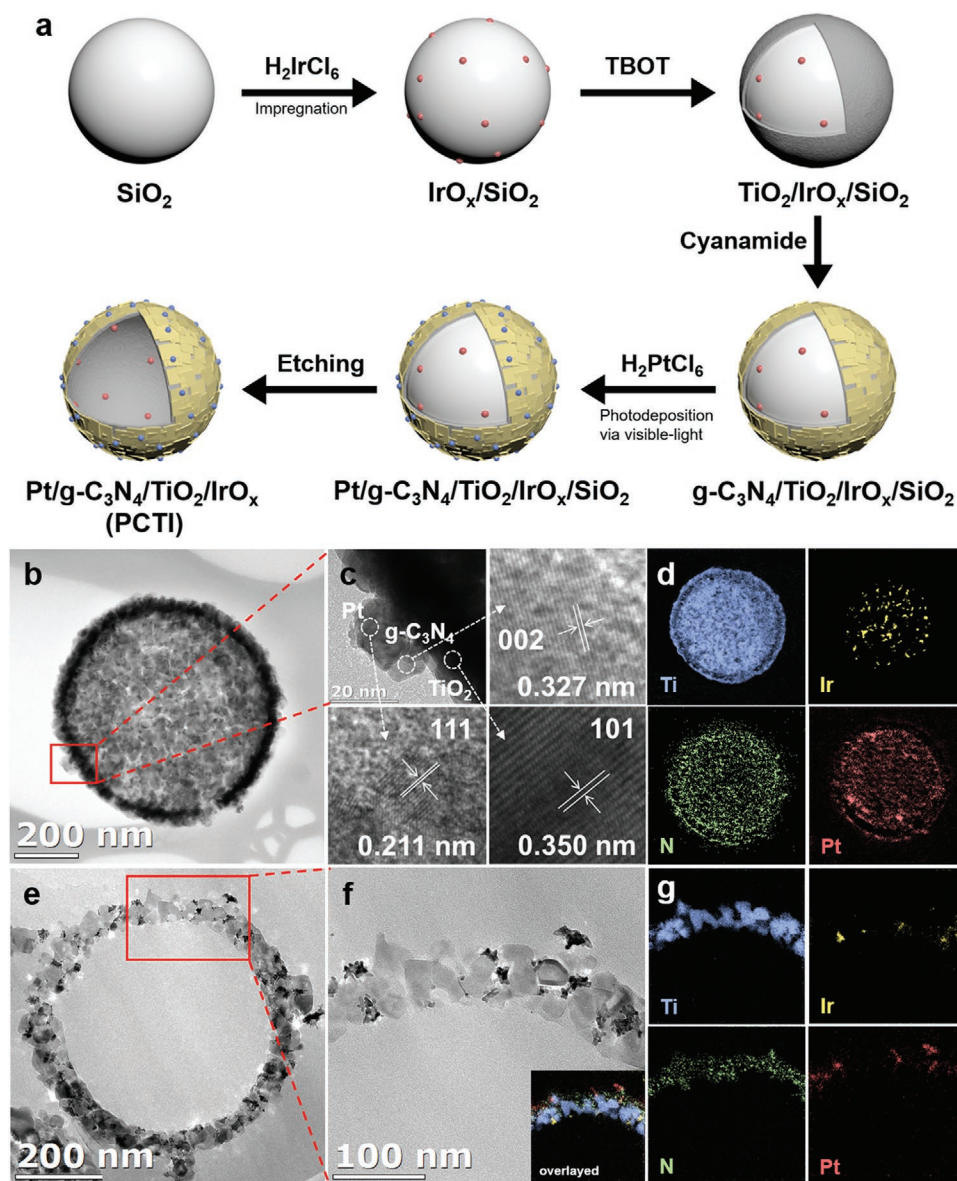


Figure 1. a) Schematic of the synthesis of PCTI. b) TEM image of PCTI. c) HRTEM image of the highlighted area in (a) and the interlayer spacing of PCTI. d) EELS elemental mapping (Ti, Ir, N, and Pt) of the PCTI hollow spheres. e) Cross-sectional TEM image of PCTI prepared using TXP and PIP. f) Magnified TEM image of the area highlighted by a red line in (e) (inset: overlay of EELS elemental mapping). g) EELS elemental mapping of the Ti, Ir, N, and Pt signals.

a thin layer and partial aggregation of $g\text{-C}_3\text{N}_4$ and Pt. Ir has a confined distribution area than the other three elements, suggesting that IrO_x was present on the inner surface of TiO_2 . The carbon distribution from $g\text{-C}_3\text{N}_4$ was not clearly observed due to the adventitious carbon source from the TEM grids (Figure S11, Supporting Information). A target surfacing system (TXP) and precision ion polishing (PIP) were used to further investigate the cross-sectional structure of PCTI. Figure 1e,f shows the corresponding cross-sectional TEM images of PCTI. The formation of a heterojunction and the spatial separation of the cocatalysts are clearly observed in the EELS elemental mapping of the PCTI hollow spheres in the cross-sectional TEM image (Figure 1g); Ti represents the framework of the hollow spheres,

and N is shallowly coated on the outer Ti surface, forming a heterojunction, while Ir and Pt are attached to the opposite surfaces of the shell.

The X-ray diffraction (XRD) pattern of the as-prepared samples in Figure S12 (Supporting Information) also describes the evolution of the structure. Bulk $g\text{-C}_3\text{N}_4$ exhibits a dominant (002) peak at $2\theta = 27.5^\circ$, which originates from the interlayer stacking,^[39] while SiO_2 exhibits a primary peak at $2\theta = 23^\circ$, which is attributed to the (011) plane. After TiO_2 deposition on the SiO_2 nanospheres, the main SiO_2 peak substantially attenuated as typical anatase TiO_2 peaks appeared, which agrees well with JCPDS 21-1272. After $g\text{-C}_3\text{N}_4$ coating, the (002) peak of $g\text{-C}_3\text{N}_4$ appeared with reduced intensity, implying a lower

weight fraction than that of bulk g-C₃N₄. Interestingly, the (002) peak shifted from 27.5° to 27.7° compared to that of bulk g-C₃N₄, indicating that the interlayer stacking distance decreased, resulting in decreased thickness and size. After etching with NaOH, the XRD pattern was identical to that of the previous step, except that the SiO₂ peak disappeared. Moreover, a drastic increase in Braunauer–Emmett–Teller surface area of g-C₃N₄/TiO₂ (CT) hollow spheres (3788 m² g⁻¹) compared to nanospheres with SiO₂ cores (≈6 m² g⁻¹) was confirmed by nitrogen adsorption measurements (Figure S13, Supporting Information). This result demonstrates that the target structures, CT hollow spheres, were successfully synthesized.

The optical properties and band structures of the CT heterojunction were determined using ultraviolet–visible diffuse reflectance spectra (UV–visible DRS) and UV photoelectron spectroscopy (UPS). As shown in Figure 2a, the TiO₂ hollow spheres only exhibited intense absorption in the UV region, while g-C₃N₄ exhibited moderate absorption in the visible-light region up to ≈450 nm. Compared to TiO₂, CT exhibited a color change to pale yellow (insets in Figure 2a) when the TiO₂ and g-C₃N₄ heterojunction was formed, resulting in a redshift in the visible-light region. The two absorption steps correspond to the intrinsic absorption of TiO₂ and g-C₃N₄. The intrinsic bandgap of the as-prepared composites was estimated from the Tauc plots in Figure 2b (i.e., the curve of converted $(\alpha h\nu)^r$ vs $h\nu$ from

the UV–vis spectrum, where α is the absorption coefficient, h is the Planck's constant, ν is the light frequency, $r = 2$ for a direct-bandgap material, such as TiO₂, and $r = 1/2$ for an indirect-bandgap material, such as g-C₃N₄).^[40,41] Thus, the intrinsic bandgaps of the TiO₂ hollow spheres and g-C₃N₄ were calculated as 3.34 and 2.70 eV, respectively, by measuring the x -axis intercept of an extrapolated line from the linear regime of the curve. From the UPS spectra in Figure 2c and Figure S14 (Supporting Information), the ionization potentials of TiO₂ and g-C₃N₄, which are equivalent to the VB energy, were calculated as -7.3 and -5.98 eV (vs vacuum), respectively, by subtracting the width of the peak from the excitation energy (21.22 eV). Subsequently, the VB energy of TiO₂ and g-C₃N₄ versus reversible hydrogen electrode (RHE) was converted to 2.86 and 1.54 eV, respectively, using the following relationship: $E_{\text{vacuum}} = -E_{\text{RHE}} - 4.44$ eV. The band positions of TiO₂ and g-C₃N₄ can then be outlined in Figure 2d using the calculated bandgap values (Figure 2b) and the measured VB energy (Figure 2c), listed in Table S1 (Supporting Information). Notably, the CB of g-C₃N₄ was sufficiently negative for efficient H₂ evolution, indicating that the g-C₃N₄ and TiO₂ heterojunction is an appropriate photocatalyst with a strong reduction ability of CB electrons, making it suitable for proton reduction.

Afterward, the Z-scheme charge-transfer pathway in the CT heterojunction was confirmed by analyzing the intermolecular

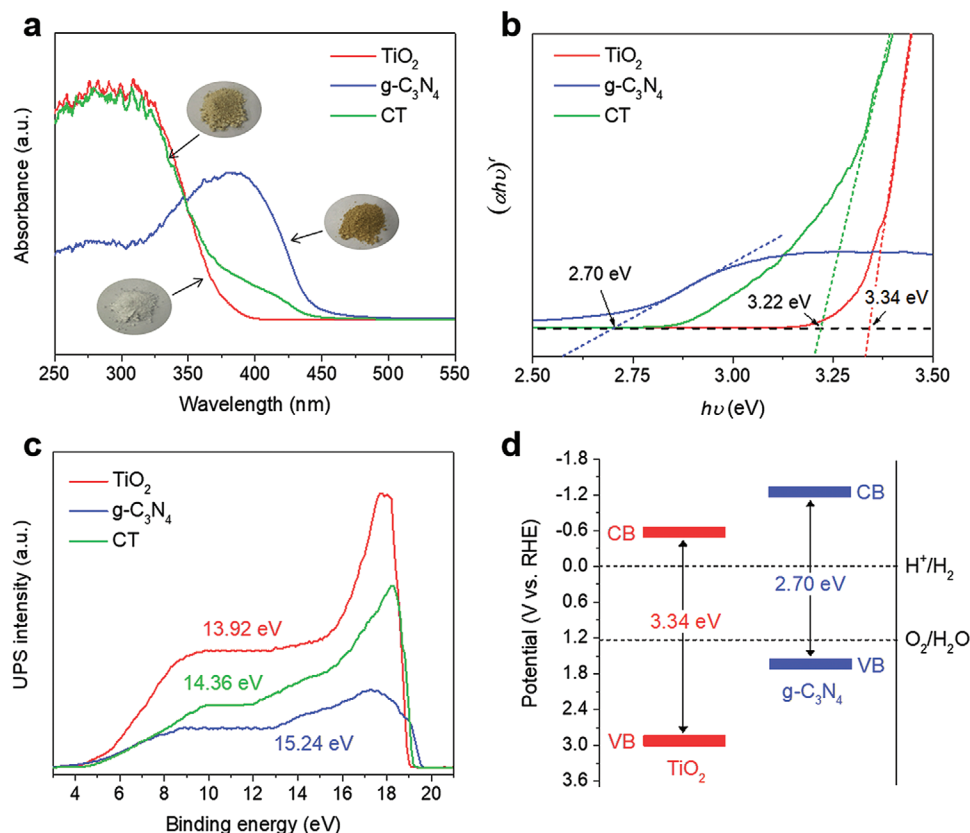


Figure 2. a) UV–visible DRS of TiO₂, g-C₃N₄, and the CT composite, where the insets show photographs of TiO₂, g-C₃N₄, and CT. b) Corresponding Tauc plots for TiO₂ and g-C₃N₄ using $(\alpha h\nu)^r$ ($r = 2$ for TiO₂ and 0.5 for g-C₃N₄) as a function of the photon energy. The intrinsic bandgaps are 3.34, 2.70, and 3.22 eV for TiO₂, g-C₃N₄, and CT, respectively. c) UPS spectra of TiO₂, g-C₃N₄, and the CT composite. The VB energy values were calculated using He I excitation energy (21.22 eV) – UPS width. d) Band structure alignments for TiO₂ and g-C₃N₄.

and electronic interaction between g-C₃N₄ and TiO₂. To demonstrate the electrostatic attraction between the components, the zeta potential of the SiO₂ and TiO₂/SiO₂ nanospheres was measured at the corresponding pH values of the synthesis step (Figure 3a). With the addition of NH₄OH, the zeta potential of the pristine SiO₂ nanospheres was measured as -33.11 mV in an ethanol solution. Hence, the Ti⁴⁺ ions can be easily adsorbed on the negatively charged sites of the SiO₂ surface via electrostatic interactions. Thereafter, cyanamide, a g-C₃N₄ precursor, which may be negatively charged owing to the presence of abundant -C-N- motifs,^[28,42] can be readily adsorbed on the positively charged TiO₂ surface (+19.36 mV). During subsequent annealing, ultrathin g-C₃N₄ was synthesized and strongly anchored on the TiO₂ surface, resulting in a CT heterostructure with intimate contact between the components.

The electron migration between g-C₃N₄ and TiO₂ in the CT heterostructure hollow spheres was also investigated using XPS, as shown in Figure S15 (Supporting Information). The high-resolution O 1s spectra of TiO₂ are fitted to three peaks at 530.2, 531.3, and 532.9 eV, which can be assigned to Ti-O, adsorbed OH⁻ species, and adsorbed molecular water or oxygen vacancies, respectively. The Ti 2p XPS spectra of TiO₂ are fitted to two peaks at 458.5 and 464.3 eV, which can be indexed to Ti 2p_{3/2} and Ti 2p_{1/2} of Ti⁴⁺, respectively. The C 1s spectra of g-C₃N₄ are fitted into three peaks at 284.6, 285.8, and 288.1 eV. The peak at 284.6 eV is assigned to the adventitious carbon and served as the reference to calibrate all the spectra. The peaks at 285.8 and 288.1 eV originate from the C=N bonds and the C-N (or C-(N)₃) bonds of the triphenylamine unit,^[43] respectively. For the N 1s spectra of g-C₃N₄, the peaks at 398.2 and 399.4 eV correspond to sp²-hybridized aromatic N (C=N-C)

and tertiary nitrogen N-(C)₃, respectively. After coupling TiO₂ with g-C₃N₄, the O 1s and Ti 2p peaks exhibited negative shifts of 0.3 and 0.2 eV in the CT hollow spheres, respectively, while the molecular water peak in O 1s disappeared because of thermal involvement during g-C₃N₄ deposition. In addition, the C 1s and N 1s core levels in the CT hollow spheres shifted positively by 0.2 and 0.3 eV, respectively. Such shifts indicate electron flow from g-C₃N₄ to TiO₂ through the interface under dark conditions.

To further verify the electron migration between g-C₃N₄ and TiO₂, their work functions (WFs) were measured using a Kelvin probe since the interfacial charge-transfer process is closely related to the WF. As shown in Figure 3b, the contact potential difference (CPD) between g-C₃N₄ and the Pt probe is -400 mV, while the CPD between TiO₂ and the Pt probe is -100 mV. Thus, using WF (eV) = 4.78 + e × CPD (where e is the charge of an electron, and the WF of the Pt probe is 4.78 eV), the WFs of g-C₃N₄ and TiO₂ were calculated as 4.38 and 4.68 eV, respectively (Figure 3c). When g-C₃N₄ and TiO₂ came into contact, the free electrons migrated from g-C₃N₄ to TiO₂ through the intimate interface until their Fermi levels were equilibrated, which is consistent with the electron flow probed by XPS analysis. At equilibrium, the electrons were accumulated on the TiO₂ interface, while the electron density decreased on the g-C₃N₄ interface. Consequently, the positively charged g-C₃N₄ and the negatively charged TiO₂ created an internal electric field that was directed from g-C₃N₄ to TiO₂ at the interface. As electrons in g-C₃N₄ were repelled by the internal electric field, the potential energy increased, and the bands bent upward; conversely, the potential energy of electrons in TiO₂ decreased, and the bands bent downward. Under irradiation, the photogenerated

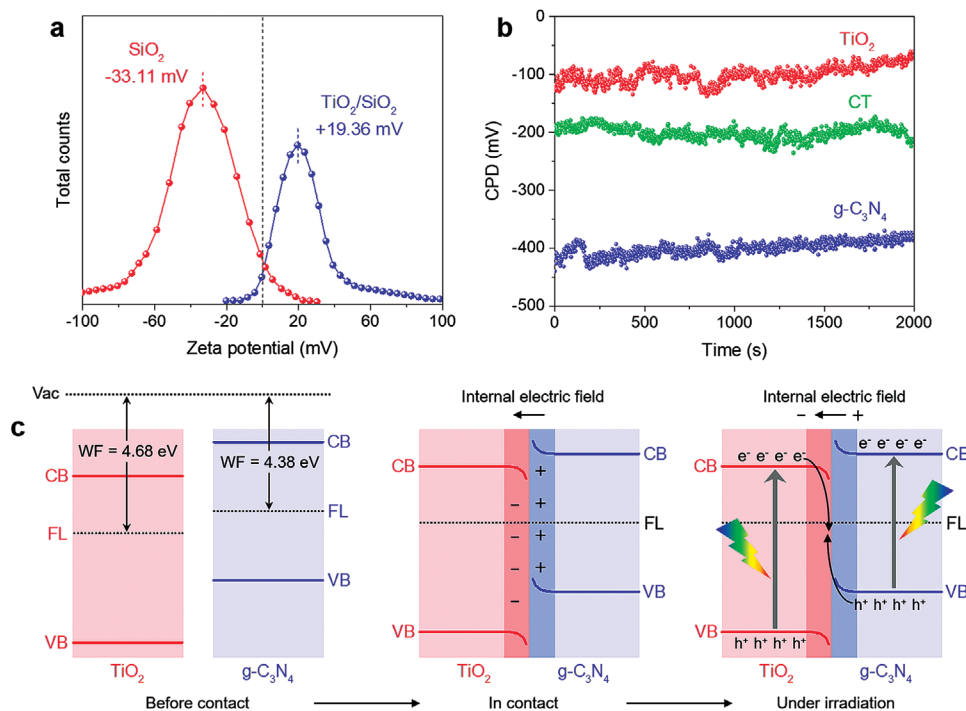


Figure 3. a) Zeta potential of the SiO₂ (at pH 9) and TiO₂/SiO₂ (at pH 4) nanospheres. b) CPD of TiO₂, g-C₃N₄, and the CT composite in the dark. c) Schematic of the Z-scheme charge-transfer process.

electrons in the CB of TiO₂ were likely to recombine with the photogenerated holes at the VB of g-C₃N₄ through the interface as driven by the internal electric field and the interfacial band bending, implying a Z-scheme charge-transfer process in the CT heterostructure hollow spheres.

For direct evidence of Z-scheme charge-transfer within the CT hollow spheres, electron spin resonance (ESR) analysis was conducted to probe the superoxide and hydroxyl radicals ($\cdot\text{O}_2^-$ and $\cdot\text{OH}$) by using 5,5-dimethyl-1-pyrroline *N*-oxide (DMPO) as the trapping agent, as shown in Figure S16 (Supporting Information). Prior to measurement, methanol/DMPO/photocatalysts ($\cdot\text{O}_2^-$) and DI/DMPO/photocatalysts ($\cdot\text{OH}$) mixtures were illuminated for 120 s. For DMPO- $\cdot\text{O}_2^-$, since the potential of $\text{O}_2/\cdot\text{O}_2^-$ is -0.33 V versus RHE at pH 7, TiO₂ (CB = -0.48 eV) exhibited weak ESR signals, while g-C₃N₄ (CB = -1.16 eV) exhibited stronger ESR signals, demonstrating the reduction potential difference between TiO₂ and g-C₃N₄. In comparison, the CT heterojunction exhibited the most intensified ESR signals, which can be attributed to the enhanced reduction ability as a result of the enhanced charge separation efficiency. For DMPO- $\cdot\text{OH}$, two oxidation reactions were considered: $\cdot\text{OH}/\text{OH}^-$ and $\cdot\text{OH}/\text{H}_2\text{O}$, which occur at 1.99 and 2.34 V versus RHE at pH 7, respectively. TiO₂, which has relatively positive VB (2.86 eV) than the potential of $\cdot\text{OH}/\text{OH}^-$ and $\cdot\text{OH}/\text{H}_2\text{O}$, exhibited ESR signals, while g-C₃N₄, which has relatively negative VB (1.54 eV) than the potential of $\cdot\text{OH}/\text{OH}^-$ and $\cdot\text{OH}/\text{H}_2\text{O}$, exhibited negligible ESR signals. CT heterojunction exhibited the intensified ESR signals, providing reliable evidence of Z-scheme charge transfer and enhanced oxidation ability. The ESR signal was not detected in dark (Figure S17, Supporting Information), indicating that these redox reactions are photoinduced process. Moreover, photo-oxidation depositions of Pb²⁺ ions on the CT heterojunction were performed with NaIO₃ as an electron acceptor to further support the Z-scheme charge-transfer pathway. As shown in Figure S18 (Supporting Information), the contrasts inside the shell were observed in the HAADF- and BF-STEM images, implying lead oxide particles were formed selectively on the TiO₂ surface. HRTEM and EELS mapping clearly demonstrated the deposited particles were lead species, specifically PbO₂. The formation of PbO₂ is an indication that photo-oxidation selectively takes place on the TiO₂ surface, i.e., the photoexcited holes migrate to TiO₂ via Z-scheme charge transfer.

To highlight the merits of spatially separated cocatalysts, CT and TiO₂ hollow spheres with different combinations of Pt and IrO_x, such as pristine CT, Pt/g-C₃N₄/TiO₂ (PCT), g-C₃N₄/TiO₂/Pt (CTP), IrO_x/g-C₃N₄/TiO₂ (ICT), g-C₃N₄/TiO₂/IrO_x (CTI), PCTI, Pt-IrO_x/g-C₃N₄/TiO₂ (PICT), g-C₃N₄/TiO₂/Pt-IrO_x (CTPI), IrO_x/g-C₃N₄/TiO₂/Pt (ICTP), Pt-IrO_x/g-C₃N₄/TiO₂/Pt-IrO_x (PICTPI), Pt/TiO₂ (PT), and Pt/TiO₂/IrO_x (PTI) hollow spheres, were synthesized (Figure 4a). Inductively coupled plasma atomic emission spectroscopy (ICP-AES) confirmed that the Pt and IrO_x contents in the as-prepared photocatalysts were constantly adjusted to 0.5 and 1.2 wt%, respectively, as summarized in Table S2 (Supporting Information). The photocatalytic activity of the as-prepared composites, as well as TiO₂ hollow spheres and bulk g-C₃N₄, was evaluated in Figure 4b and Figure S19 (Supporting Information) by monitoring H₂ evolution in an aqueous solution containing methanol (MeOH) as a sacrificial agent under simulated solar illumination. As

expected, neither TiO₂ hollow spheres nor bulk g-C₃N₄ were capable of proton reduction, however, the heterojunction photocatalyst, CT, was capable of splitting water for H₂ evolution without any cocatalyst due to the interfacial Z-scheme charge transfer. When IrO_x was loaded on the CT heterostructure hollow spheres (ICT and CTI in Figure 4a), a trace amount of H₂ was produced due to the low hydrogen evolution activity of IrO_x. Interestingly, the Pt-only-loaded CT hollow spheres (PCT and CTP in Figure 4a) exhibited higher H₂ evolution performance than the samples loaded with the dual cocatalysts on the same surface (PICT, CTPI, and PICTPI in Figure 4a), implying that the random distribution of the cocatalysts induced more charge recombination. As a result, PICTPI, in which dual cocatalysts were randomly deposited on both sides, exhibited the lowest H₂ evolution activity among the as-prepared CT photocatalysts. Furthermore, the loading of Pt on g-C₃N₄ (PCT, PCTI, and PICT in Figure 4a) resulted in a relatively higher H₂ evolution performance than that of the counterpart samples (CTP, ICTP, and CTPI in Figure 4a), indicating that the loading position of cocatalysts along the Z-scheme charge-transfer pathway is also critical for photocatalytic activity. Meanwhile, PCTI, in which Pt and IrO_x were separately deposited on g-C₃N₄ and TiO₂, respectively, exhibited the highest H₂ evolution performance of 8.15 mmol h⁻¹ g⁻¹ due to the cooperation of the Z-scheme heterostructures and the spatially separated cocatalysts. To optimize the sacrificial reagent as an electron donor, methanol and triethanolamine (TEOA) were employed in the PCTI system because methanol and TEOA are well-known sacrificial agents for TiO₂ and g-C₃N₄, respectively. Figure S20 (Supporting Information) shows that the PCTI in the aqueous methanol solution has a higher H₂ evolution activity than that in the aqueous TEOA solution (5.92 mmol h⁻¹ g⁻¹), demonstrating a Z-scheme charge-transfer pathway within the system, which causes the accumulation of photoexcited holes in the VB of TiO₂. The accumulated holes at TiO₂ can then be readily removed by methanol, resulting in a superior H₂ evolution activity over the case of using TEOA.

The photocatalytic stability of the optimized sample, PCTI, was also investigated. As shown in Figure 4c, no noticeable degradation in photocatalytic activity was observed during the four reaction cycles (8 h per cycle) and the last cycle maintained $\approx 92\%$ of the H₂ evolution rate of the first cycle. This outcome signifies that the PCTI heterostructure hollow sphere is very stable for the proton reduction reaction. The almost identical TEM images, XRD patterns, and XPS spectra before and after the long-term photocatalytic reaction (Figures S21 and S22, Supporting Information) further demonstrate the excellent physical and chemical stability of PCTI hollow spheres for H₂ evolution. Also, it is noteworthy that the TiO₂ to g-C₃N₄ mass ratios and the amounts of Pt and IrO_x loaded on the PCTI as cocatalysts remained nearly unchanged, as confirmed by ICP-AES (Tables S3 and S4, Supporting Information). These results indicate that the system in which the Pt and IrO_x cocatalysts were loaded on the electrostatically assembled CT heterostructure remained robust during the photocatalytic reaction process.

To attentively investigate the synergistic effect of Z-scheme heterojunction and spatially separated cocatalysts, the single-photocatalyst system, PT (standard) and PTI (spatially separated cocatalysts) (Figure 4a), were compared with the Z-scheme

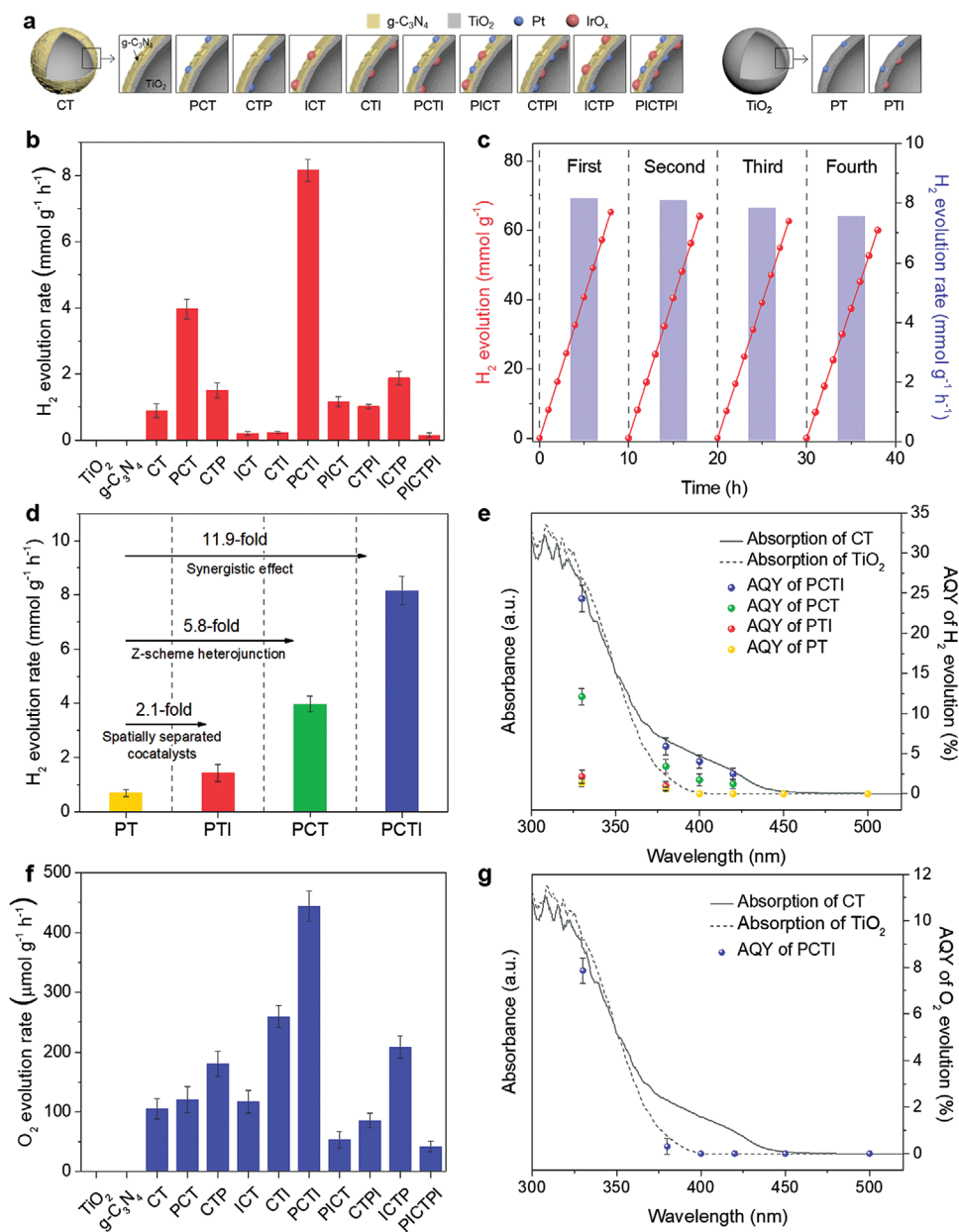


Figure 4. a) Schematic of various combinations of cocatalyst deposition on the CT and TiO₂ hollow spheres. b) Comparison of H₂ evolution rates of the as-prepared photocatalysts in 20 mL of 10 vol% aqueous MeOH solution under full-spectrum irradiation. c) Cycling of photocatalytic H₂ evolution of PCTI, where each cycle was started with a 1 h argon flush. d) Comparison of H₂ evolution rates of PCTI, PCT, PTI, and PT. e) Wavelength-dependent AQY for photocatalytic H₂ evolution and light absorption spectrum of PCTI, PCT, PTI, and PT. f) Comparison of O₂ evolution rates of the as-prepared photocatalysts in 20 mL of 0.01 M AgNO₃ aqueous solution under full-spectrum irradiation. g) Wavelength-dependent AQY for photocatalytic O₂ evolution and light absorption spectrum of PCTI.

heterojunction system, PCT (Z-scheme heterojunction) and PCTI (spatially separated cocatalysts on Z-scheme heterojunction). As shown in Figure 4d and Figure S23 (Supporting Information), the Pt-loaded TiO₂ hollow spheres (PT) exhibited only 0.68 mmol g⁻¹ h⁻¹ of H₂ evolution rate. Compared with PT, PTI exhibited a 2.1-fold increased H₂ evolution rate (1.43 mmol g⁻¹ h⁻¹) due to the spatially separated cocatalysts, while PCT exhibited a 5.8-fold increased H₂ evolution rate (3.97 mmol g⁻¹ h⁻¹) due to the Z-scheme charge transfer between g-C₃N₄ and TiO₂. In comparison, PCTI exhibited an 11.9-fold increased H₂ evolution rate

compared to that of PT. This increase of H₂ evolution activity was not a simple addition of the individual increase from the Z-scheme heterojunction and the spatially separated cocatalysts, strongly suggesting the validity of synergistic effect of the two aspects. Such a synergy was also evidently seen in the comparison of apparent quantum yield (AQY), as shown in Figure 4e. The consistency between the optical absorption and the AQY at different wavelengths further suggests that this water-splitting reaction was indeed driven by light absorption by the photocatalysts. Due to the negligible visible-light absorption

of TiO₂, the AQY values were compared at 330 nm and the calculated AQY values were 1.03%, 2.14%, 12.1%, and 24.3% for PT, PTI, PCT, and PCTI, respectively. For PT and PTI, the equation for the one-step excitation process was used, and for PCT and PCTI, the equation for the two-step excitation process was used, which is typically considered for Z-scheme systems.^[44] Owing to the synergistic effect of Z-scheme heterojunction and spatially separated cocatalysts, the AQY of PCTI at 330 nm was enhanced by ≈24-fold compared to that of PT, surpassing the addition of the AQY enhancement from PTI (≈1.9-fold) and PCT (≈11.7-fold). Also, PCTI outperforms most previously reported g-C₃N₄/TiO₂ heterostructure photocatalysts in terms of H₂ evolution rate and AQY (Table S5, Supporting Information). The AQY of PCTI at 420 nm was calculated to be 2.49%, which is not as excellent as the AQY at 330 nm. This can be ascribed to the poor photon harvesting of TiO₂ under visible-light irradiation, resulting in an invalid Z-scheme charge transfer within the PCTI system.

Additionally, for overall water splitting feasibility, the O₂ evolution reaction was conducted over PCTI. Negligible activity of O₂ evolution was observed without any sacrificial reagent (Figure S24, Supporting Information), because the short hole diffusion length of TiO₂ (≈1–10 nm)^[45,46] restricts the hole shift in the quasi-Fermi level under photoexcitation.^[27] In the presence of sacrificial electron acceptors of AgNO₃, the hole diffusion length was elongated enough to induce O₂ evolution reaction, however, the gradual decrease was observed due to the ongoing deposition of Ag resulting in the blockage of the photocatalyst surface. Figure 4f shows the O₂ evolution rate of as-prepared photocatalysts in an aqueous solution containing 0.01 M AgNO₃ during the first hour of simulated irradiation. With a trend similar to H₂ evolution, PCTI exhibited the highest O₂ evolution performance (443.9 μmol g⁻¹ h⁻¹) compared to the counterpart samples, demonstrating the synergistic effect of Z-scheme charge transfer and spatially separated cocatalysts was also valid for O₂ evolution. The photocatalysts in which IrO_x was deposited on TiO₂ induced higher O₂ performance than that of the counterpart samples, proving again the importance of loading position of cocatalysts. As shown in Figure 4g, it is noticeable that the AQY profile of O₂ evolution is consistent with the optical absorption of TiO₂ rather than CT heterojunction, strongly indicating that the O₂ evolution reaction was induced by holes in TiO₂ as a consequence of the Z-scheme charge-transfer pathway. The AQY at 330 nm was calculated to be 789% using the equation for the dual-photon Z-scheme photocatalytic system, which surpasses most previously reported TiO₂-based photocatalysts in terms of O₂ evolution rate and AQY (Table S6, Supporting Information).

The scenario of charge-transfer dynamics was further investigated to elucidate the mechanistic origins underlying the superior H₂ evolution performance of PCTI. In particular, the dependence of interfacial charge transfer of CT on the location of the loaded cocatalysts was explored in order to reveal the beneficial role of spatially separated cocatalysts. Figure 5a shows the steady-state photoluminescence (PL) emission spectra of pristine CT and CT loaded with cocatalysts under six different situations. The pristine CT without cocatalysts exhibited a prominent PL emission band centered around 470 nm. Upon loading cocatalysts, the PL intensity of CT was greatly depressed, suggesting the localized charge carriers of CT can be further transported to

the loaded cocatalysts. Among the six cocatalysts-loaded CT samples, PCTI exhibited the most dramatic PL quenching indicative of the most effective charge separation. This finding implies that loading dual cocatalysts at specific surfaces of CT, i.e., Pt at g-C₃N₄ and IrO_x at TiO₂, can inhibit the radiative recombination of charge carriers to the largest extent, thus giving rise to the most pronounced charge-carrier separation. To obtain quantitative index of interfacial charge transfer, time-resolved PL (TRPL) spectra were further measured at the corresponding steady-state emission peaks (Figure 5b). These decay profiles were fitted with a triexponential kinetics equation (Table S6, Supporting Information). The intensity-average PL lifetime (τ_{avg}) was then computed to make an overall comparison. As compared to pristine CT ($\tau_{\text{avg}} = 21.1$ ns), the six cocatalysts-loaded CT samples all displayed a shortened average PL lifetime, with the PCTI having the shortest value ($\tau_{\text{avg}} = 7.2$ ns). By assuming that charge transfer from CT to the loaded cocatalysts accounts for the observed rapid PL decay kinetics of cocatalysts-loaded samples, the rate constant of interfacial charge transfer (k_{ct}) can be computed for comparison. Among the six cocatalysts-loaded CT samples, PCTI showed the highest k_{ct} value of 9.14×10^7 s⁻¹, reflecting the most pronounced charge separation efficiency. The trends of PL emission quenching and k_{ct} variation among the six cocatalysts-loaded CT photocatalysts were consistent with the results of photocatalytic H₂ evolution performance, validating a direct correlation between charge separation efficiency and photocatalytic activity. This consistency also discloses the beneficial role of spatially separated cocatalysts in enhancing surface charge separation for expediting reaction kinetics.

The charge-transfer dynamics of cocatalysts-loaded CT samples were further evaluated by photoelectrochemical measurements. Figure 5c shows the photoelectric response upon repeated on/off illumination cycles, revealing the substantially higher transient photocurrent density of PCTI than the other cocatalysts-loaded CT samples. The prevalence of pronounced surface charge separation of PCTI in which the photogenerated electrons were trapped at Pt on the external surface of CT and the photoexcited holes were trapped at IrO_x on the internal surface of CT was favorable performing water redox reaction. Also, the electrochemical impedance spectroscopy (EIS) Nyquist plots fitted by an equivalent circuit model in Figure 5d and Table S8 (Supporting Information) reveal PCTI exhibits a much decreased charge-transfer resistance ($R_{\text{ct}} = 1.52$ kΩ) than that of the other cocatalysts-loaded CT samples, indicating the faster charge-transfer process in PCTI. These results further demonstrate the benefits of spatially separating cocatalysts for efficient charge separation and transfer.

Photo-KPFM analysis was conducted to further investigate the spatial charge separation in PCTI under irradiation. Figure 6a–c shows mapping images of the topography and surface potential (SP) with and without UV-B light irradiation of PCTI. To examine the evolution of the SP along the structural transformation, photo-KPFM analysis was also conducted on TI and CTI, as depicted in Figure S25 (Supporting Information), and the measured SPs are summarized in Table S9 (Supporting Information). Figure 6d shows the calculated SP difference (ΔSP), which can be employed to investigate the photoresponse and the photogenerated electron–hole pairs in the photocatalyst. Generally, as light strikes a semiconductor, the photoexcited

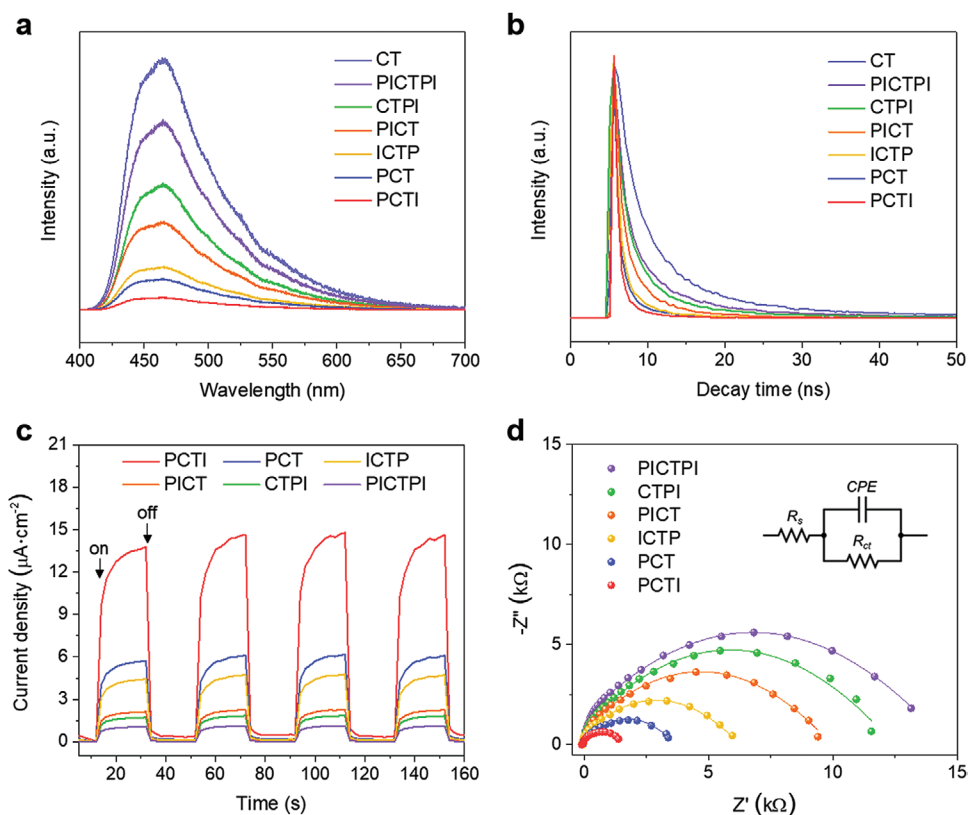


Figure 5. a) Steady-state PL emission spectra and b) TRPL decay spectra of the as-prepared photocatalysts at room temperature. The excitation wavelength for all samples is 375 nm. c) Transient photocurrent density curves of the as-prepared photocatalysts at 0.0 V versus Ag/AgCl in aqueous 0.5 m Na₂SO₄ solution under sequential illumination conditions with an interval of 20 s on/off switch. d) EIS Nyquist plots of the as-prepared photocatalysts at 0.6 V versus Ag/AgCl in aqueous 0.5 m Na₂SO₄ solution under light irradiation, where the inset is an equivalent circuit for the catalyst/electrolyte interfaces: R_s is the electrolyte resistance. R_{ct} and CPE is the charge-transfer resistance from the bulk to the surface of photocatalyst and the constant phase element, respectively.

electrons accumulate at the surface of the material, causing the SPs to shift negatively. In contrast, a decrease in electron density causes a positive shift in the SP of materials. Thus, the increased SP ($\Delta SP = 40$ mV) of TI after light illumination indicates a reduction in the electron density at the surface compared to the conditions in the dark. This suggests that electrons were transferred from the external TiO₂ shell to the internal IrO_x particles due to the large work function of IrO_x.^[47] However, after TI formed a heterojunction with g-C₃N₄, CTI exhibited a significantly attenuated SP shift compared to TI upon light irradiation ($\Delta SP = 6$ mV), which is indicative of a diminution in the inward migration of electrons due to the Z-scheme charge transfer and the accumulation of photoexcited electrons on the outermost g-C₃N₄ layer. PCTI exhibited a distinctive negative SP shift upon light irradiation ($\Delta SP = -33$ mV), indicating that the photoexcited electrons migrated to the external PCTI surface, g-C₃N₄, and were preferentially trapped by the Pt cocatalysts.

The H₂ evolution performance is determined by the photo-generated carrier separation and migration efficiency and the surface reaction rate. The outstanding H₂ evolution rate (8.15 mmol g⁻¹ h⁻¹) of PCTI can be ascribed to the improved charge separation and migration efficiency in both the bulk phase and at the surface due to the synergy of the Z-scheme CT heterostructure and the separately loaded cocatalysts, as depicted in Figure 6e,f. In the case of Z-scheme charge transfer within

the PCTI heterojunction, a built-in electric field was created near the junction due to the mismatched Fermi energy levels, and this electric field accumulated the electrons and holes at the interfaces, resulting in band bending. Owing to the internal electric field and interfacial band bending, the photogenerated electrons and holes could be efficiently separated and transported, retaining the strong reduction and oxidation ability (the electrons and holes in the CB of g-C₃N₄ and the VB of TiO₂, respectively). Additionally, separately loading Pt and IrO_x on the surfaces of the hollow spheres accelerated the surface reaction kinetics because the cocatalysts can reduce surface recombination and decrease the activation energy of reduction and oxidation reactions in water splitting. If Pt and IrO_x are loaded randomly on both sides, e.g., the Pt on the TiO₂ side and the IrO_x on the g-C₃N₄ side, they would not facilitate surface reaction kinetics to promote reaction rate, and even worse, they can induce the reverse reactions to retard water splitting. Thus, loading Pt and IrO_x on the g-C₃N₄ and TiO₂ surfaces, respectively, can greatly improve the photocatalytic H₂ evolution activity.

3. Conclusion

Z-scheme CT heterostructure hollow spheres were successfully synthesized by growing ultrathin g-C₃N₄ on the surface of

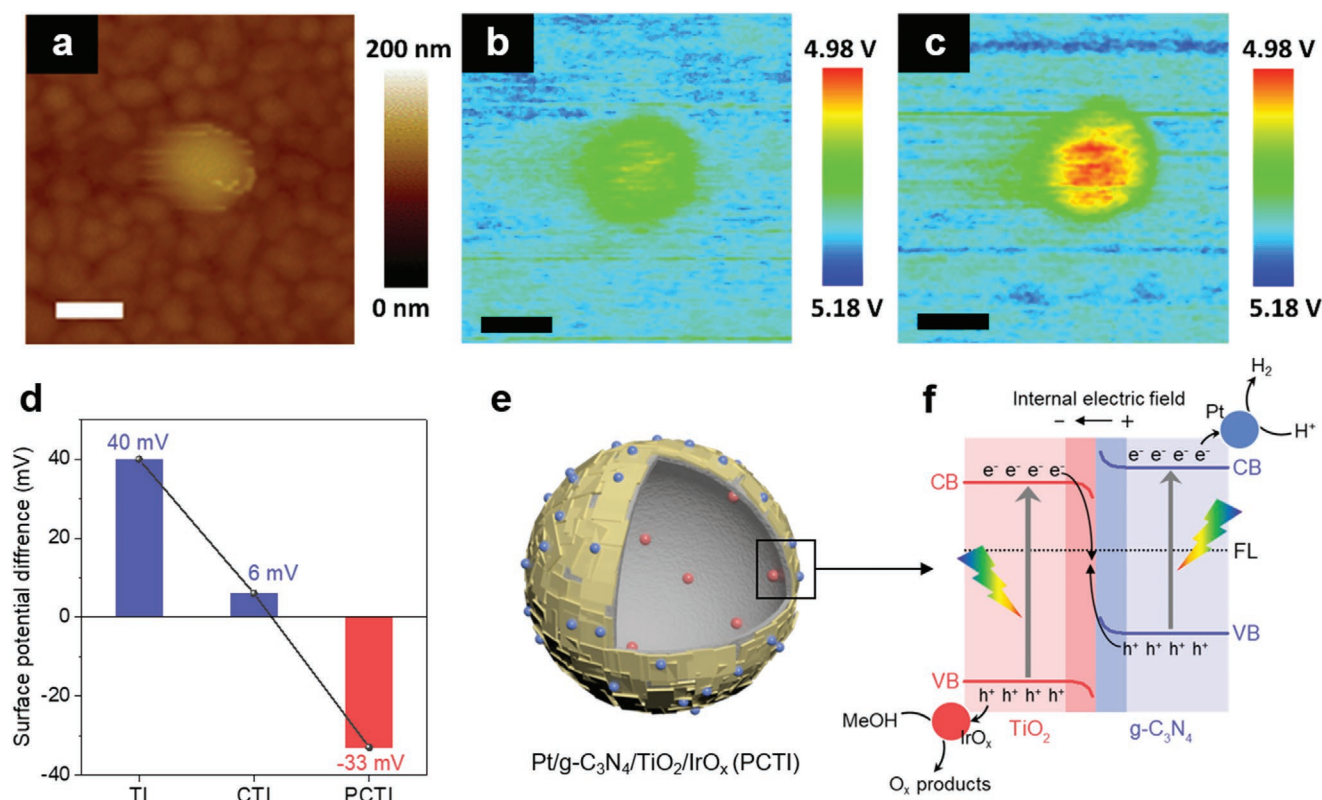


Figure 6. a) KPFM topography mapping of PCTI. b,c) Corresponding SP mapping of PCTI in darkness (b) and under light irradiation (c). d) Calculated Δ SP according to the structure evolution. e) Illustration of the physical structure of PCTI. f) Schematic of the charge-transfer process within PCTI upon light irradiation.

TiO₂ nanospheres via electrostatic interactions. In addition to the Z-scheme heterostructure, spatial separation of cocatalysts was employed to suppress photogenerated charge recombination on the surface and enhance the surface reaction kinetics. The as-prepared PCTI hollow sphere photocatalyst exhibited the highest H₂ evolution rate of 8.15 mmol h⁻¹ g⁻¹ and a prominent AQY of 24.3% at 330 nm in the presence of 0.5 wt% Pt and 1.2 wt% IrO_x cocatalysts on g-C₃N₄ and TiO₂, respectively. Photo-KPFM analysis was conducted to investigate the charge-transfer mechanism, which includes the interfacial Z-scheme pathway and the cocatalytic capture of the separated electrons and holes. According to the rational analyses, the exceptional photocatalytic performance can be mainly attributed to the synergistic effect of the formation of Z-scheme heterostructure hollow spheres and the spatial separation of the cocatalysts, which resulted in efficient charge separation and transfer in both the bulk phase and at the surface. This work adequately demonstrates that the synergy of Z-scheme heterostructures and spatial separation of cocatalysts can be a promising strategy for designing high-performance photocatalyst platforms for solar fuel production.

Supporting Information

Supporting Information is available from the Wiley Online Library or from the author.

Acknowledgements

This work was supported by the National Research Foundation of Korea (NRF) grant funded by the Korea government(MSIT) (NRF-2021R1A5A1084921, NRF-2021K1A4A8A02079226).

Conflict of Interest

The authors declare no conflict of interest.

Data Availability Statement

Research data are not shared.

Keywords

g-C₃N₄/TiO₂, photocatalytic water splitting, solar hydrogen energy, spatial separation of cocatalysts, Z-scheme heterojunctions

Received: January 7, 2022

Revised: February 9, 2022

Published online:

[1] A. J. Bard, M. A. Fox, *Acc. Chem. Res.* **1995**, *28*, 141.

[2] G. Liao, Y. Gong, L. Zhang, H. Gao, G. J. Yang, B. Fang, *Energy Environ. Sci.* **2019**, *12*, 2080.

- [3] C. Gao, T. Wei, Y. Zhang, X. Song, Y. Huan, H. Liu, M. Zhao, J. Yu, X. Chen, *Adv. Mater.* **2019**, *31*, 1806596.
- [4] H. S. Moon, K. Yong, *Appl. Surf. Sci.* **2020**, *530*, 147215.
- [5] S. Guo, Y. Li, S. Tang, Y. Zhang, X. Li, A. J. Sobrido, M.-M. Titirici, B. Wei, *Adv. Funct. Mater.* **2020**, *30*, 2003035.
- [6] L. Buzzetti, G. E. M. Crisenza, P. Melchiorre, *Angew. Chem., Int. Ed.* **2019**, *58*, 3730.
- [7] S. Wang, Y. Wang, S. L. Zhang, S.-Q. Zang, X. W. Lou, *Adv. Mater.* **2019**, *31*, 1903404.
- [8] Y. Chao, P. Zhou, N. Li, J. Lai, Y. Yang, Y. Zhang, Y. Tang, W. Yang, Y. Du, D. Su, Y. Tan, S. Guo, *Adv. Mater.* **2019**, *31*, 1807226.
- [9] B. Weng, M.-Y. Qi, C. Han, Z.-R. Tang, Y.-J. Xu, *ACS Catal.* **2019**, *9*, 4642.
- [10] Y. Lu, X.-L. Liu, L. He, Y.-X. Zhang, Z.-Y. Hu, G. Tian, X. Cheng, S.-M. Wu, Y.-Z. Li, X.-H. Yang, L.-Y. Wang, J.-W. Liu, C. Janiak, G.-G. Chang, W.-H. Li, G. Van Tendeloo, X.-Y. Yang, B.-L. Su, *Nano Lett.* **2020**, *20*, 3122.
- [11] J. Kosco, M. Bidwell, H. Cha, T. Martin, C. T. Howells, M. Sachs, D. H. Anjum, S. G. Lopez, L. Zou, A. Wadsworth, W. Zhang, L. Zhang, J. Tellam, R. Sougrat, F. Laquai, D. M. DeLongchamp, J. R. Durrant, I. McCulloch, *Nat. Mater.* **2020**, *19*, 559.
- [12] C. Cai, Y. Teng, J.-H. Wu, J.-Y. Li, H.-Y. Chen, J.-H. Chen, D.-B. Kuang, *Adv. Funct. Mater.* **2020**, *30*, 2001478.
- [13] S. Khan, H. Choi, D. Kim, S. Y. Lee, Q. Zhu, J. Zhang, S. Kim, S.-H. Cho, *Chem. Eng. J.* **2020**, *395*, 125092.
- [14] H. Gong, Z. Li, Z. Chen, Q. Liu, M. Song, C. Huang, *ACS Appl. Nano Mater.* **2020**, *3*, 3665.
- [15] C. Cheng, B. He, J. Fan, B. Cheng, S. Cao, J. Yu, *Adv. Mater.* **2021**, *33*, 2100317.
- [16] D. Zhao, Y. Wang, C.-L. Dong, Y.-C. Huang, J. Chen, F. Xue, S. Shen, L. Guo, *Nat. Energy* **2021**, *6*, 388.
- [17] B.-J. Ng, L. K. Putri, X. Y. Kong, Y. W. Teh, P. Pasbakhsh, S.-P. Chai, *Adv. Sci.* **2020**, *7*, 1903171.
- [18] X. Chen, J. Wang, Y. Chai, Z. Zhang, Y. Zhu, *Adv. Mater.* **2021**, *33*, 2007479.
- [19] X. Wang, X. Wang, J. Huang, S. Li, A. Meng, Z. Li, *Nat. Commun.* **2021**, *12*, 4112.
- [20] Q. Liu, J. Huang, L. Wang, X. Yu, J. Sun, H. Tang, *Sol. RRL* **2021**, *5*, 2000504.
- [21] D. Wang, X.-Q. Gong, *Nat. Commun.* **2021**, *12*, 158.
- [22] Z. Pan, R. Yanagi, Q. Wang, X. Shen, Q. Zhu, Y. Xue, J. A. Röhr, T. Hisatomi, K. Domen, S. Hu, *Energy Environ. Sci.* **2020**, *13*, 162.
- [23] K. Maeda, A. Xiong, T. Yoshinaga, T. Ikeda, N. Sakamoto, T. Hisatomi, M. Takashima, D. Lu, M. Kanehara, T. Setoyama, T. Teranishi, K. Domen, *Angew. Chem., Int. Ed.* **2010**, *49*, 4096.
- [24] X. Zong, H. Yan, G. Wu, G. Ma, F. Wen, L. Wang, C. Li, *J. Am. Chem. Soc.* **2008**, *130*, 7176.
- [25] K. Maeda, K. Domen, *J. Phys. Chem. Lett.* **2010**, *1*, 2655.
- [26] J. Yang, H. Yan, X. Wang, F. Wen, Z. Wang, D. Fan, J. Shi, C. Li, *J. Catal.* **2012**, *290*, 151.
- [27] D. Wang, T. Hisatomi, T. Takata, C. Pan, M. Katayama, J. Kubota, K. Domen, *Angew. Chem., Int. Ed.* **2013**, *52*, 11252.
- [28] A. Li, T. Wang, X. Chang, W. Cai, P. Zhang, J. Zhang, J. Gong, *Chem. Sci.* **2016**, *7*, 890.
- [29] R. Li, F. Zhang, D. Wang, J. Yang, M. Li, J. Zhu, X. Zhou, H. Han, C. Li, *Nat. Commun.* **2013**, *4*, 1432.
- [30] S. Obregón, G. Colón, *Appl. Catal., B* **2014**, *144*, 775.
- [31] J. Zhang, Z. Yu, Z. Gao, H. Ge, S. Zhao, C. Chen, S. Chen, X. Tong, M. Wang, Z. Zheng, Y. Qin, *Angew. Chem., Int. Ed.* **2017**, *56*, 816.
- [32] D. Zheng, X.-N. Cao, X. Wang, *Angew. Chem., Int. Ed.* **2016**, *128*, 11684.
- [33] A. C. Arango, L. R. Johnson, V. N. Bliznyuk, Z. Schlesinger, S. A. Carter, H.-H. Hörhold, *Adv. Mater.* **2000**, *12*, 1689.
- [34] G. E. Eperon, S. D. Stranks, C. Menelaou, M. B. Johnston, L. M. Herz, H. J. Snaith, *Energy Environ. Sci.* **2014**, *7*, 982.
- [35] S. D. Stranks, G. E. Eperon, G. Grancini, C. Menelaou, M. J. P. Alcocer, T. Leijtens, L. M. Herz, A. Petrozza, H. J. Snaith, *Science* **2013**, *342*, 341.
- [36] Z. Wang, W. Wu, Q. Xu, G. Li, S. Liu, X. Jia, Y. Qin, Z. L. Wang, *Nano Energy* **2017**, *38*, 518.
- [37] M. Hatanaka, N. Takahashi, N. Takahashi, T. Tanabe, Y. Nagai, A. Suda, H. Shinjoh, *J. Catal.* **2009**, *266*, 182.
- [38] P. Li, L. Kong, J. Liu, J. Yan, S. Liu, *ACS Sustainable Chem. Eng.* **2019**, *7*, 17941.
- [39] H. Huang, K. Xiao, N. Tian, F. Dong, T. Zhang, X. Du, Y. Zhang, *J. Mater. Chem. A* **2017**, *5*, 17452.
- [40] Y. Xu, S.-P. Gao, *Int. J. Hydrogen Energy* **2012**, *37*, 11072.
- [41] J. Liu, Y. Liu, N. Liu, Y. Han, X. Zhang, H. Huang, Y. Lifshitz, S. T. Lee, J. Zhong, Z. Kang, *Science* **2015**, *347*, 970.
- [42] M. S. Vohra, J. Lee, W. Choi, *J. Appl. Electrochem.* **2005**, *35*, 757.
- [43] X. Song, Y. Hu, M. Zheng, C. Wei, *Appl. Catal., B* **2016**, *182*, 587.
- [44] Z. Wang, C. Li, K. Domen, *Chem. Soc. Rev.* **2019**, *48*, 2109.
- [45] P. Salvador, *J. Appl. Phys.* **1984**, *55*, 2977.
- [46] W. H. Leng, P. R. F. Barnes, M. Juozapavicius, B. C. O'Regan, J. R. Durrant, *J. Phys. Chem. Lett.* **2010**, *1*, 967.
- [47] E. Willinger, C. Massué, R. Schlögl, M. G. Willinger, *J. Am. Chem. Soc.* **2017**, *139*, 12093.